

Article

Study on Failure Criteria and the Numerical Simulation Method of a Coal-Based Carbon Foam under Multiaxial Loading

Qikai Zhuang¹, Xiaoquan Cheng¹ , Peijie Yue¹, Xin Guo¹ and Kai Li^{2,*}

¹ School of Aeronautic Science and Engineering, Beihang University, Beijing 100191, China; zhuangqikai@126.com (Q.Z.); xiaoquan_cheng@buaa.edu.cn (X.C.); 15652581776@163.com (P.Y.); gxdfxx@163.com (X.G.)

² State Key Laboratory of NBC Protection for Civilian, Research Institute of Chemical Defense, Beijing 100191, China

* Correspondence: 750455@sohu.com

Abstract: Coal-based carbon foam (CCF) has broad application prospects in aerospace, composite material tooling and other fields. However, the lack of failure criteria limits its promotion. In previous studies, the failure criteria of similar materials were proposed, but there are some limitations. This paper proposes improved failure criteria based on macro-mechanical tests. Furthermore, uniaxial and multiaxial loading tests were carried out to obtain accurate failure criteria of CCF. Finally, 3-points bending tests of the CCF sandwich structure were conducted and their finite element models (FEMs) were established. The CCF test results show that the mechanical properties of CCF are transversely isotropic. The failure criteria in this paper can accurately predict the stress when the CCF fails. The error band boundary formula caused by the dispersion of the material were also given. The maximum load P_{\max} calculated by the failure surface (3684 N) was only 4.7% larger than the mean value measured by the test (3518 N), and all of the P_{\max} measured by the test (3933 N, 3640 N, 3657 N, 3269 N, 3091 N) were between the maximum value (4297 N) and minimum value (3085 N) calculated by the error band boundary formula, which means that the failure criteria have good precision.

Keywords: coal-based carbon foam; transverse isotropy; failure criteria; modified equivalent von Mises stress



Citation: Zhuang, Q.; Cheng, X.; Yue, P.; Guo, X.; Li, K. Study on Failure Criteria and the Numerical Simulation Method of a Coal-Based Carbon Foam under Multiaxial Loading. *Aerospace* **2023**, *10*, 721. <https://doi.org/10.3390/aerospace10080721>

Academic Editor: Kyungil Kong

Received: 17 June 2023

Revised: 14 August 2023

Accepted: 15 August 2023

Published: 17 August 2023



Copyright: © 2023 by the authors. Licensee MDPI, Basel, Switzerland. This article is an open access article distributed under the terms and conditions of the Creative Commons Attribution (CC BY) license (<https://creativecommons.org/licenses/by/4.0/>).

1. Introduction

Coal-based carbon foam (CCF) is a high-temperature-resistant foam with good comprehensive performance [1–3]. Its comprehensive performance makes it suitable for the hypersonic aircraft's thermal protection system (TPS). The Parker Solar Probe has already used CCF as its TPS material [4,5], and many projects and scholars [6–12] have also widely studied other styles of carbon foam TPS. The thermal expansion coefficient of CCF is similar to Invar, which can be used to manufacture high-precision composite material forming tooling. In contrast, the cost of CCF tooling is about 50% lower than Invar [13,14]. CCF also has a broad application prospect in other structures [2], which makes CCF great value to research.

Failure analysis is an essential part of precise CCF structural design, which requires the clarification of the mechanical properties and failure criteria of CCF. Sih et al. [15] measured the compression and shear properties of CCFs provided by different manufacturers and found that they all exhibit transverse isotropy: the mechanical properties in the foaming direction are significantly different from those perpendicular to the foaming direction. K. Li et al. [16] used the space frame matrix and tetrakaidecahedron element methods to establish a mesoscopic mechanical model of the three-dimensional open-cell CCF. They found that the CCF's elastic properties depended on the material's relative density, the shape and size of the ligament section, and Young's modulus and Poisson's

ratio. Sihn et al. [17] established representative cells of the three-dimensional mesostructures based on the essential characteristics of the CCF mesostructure and found that the bending properties of the ligament mainly determine the elastic properties of the foam; Young's modulus is mainly determined by the transverse Young's modulus of the ligament. Other scholars [18–20] have also researched the mechanical properties of CCF based on the mesoscopic model. The CCF mechanical properties measured in the previous literatures were summarized in Table 1. There were also several scholars [21–23] who used the mesoscopic model to study the thermal performance of CCF. However, they all focus on the damage research of the mesoscopic structure. There are no failure criteria suitable for macroscopic mechanical analysis. The calculation of the mesoscopic model is too large, and the mechanical parameters of the mesoscopic structure are difficult to measure, which makes its application in the failure analysis of the complex CCF structure inconvenient. Therefore, it is necessary to establish failure criteria based on the macroscopic mechanical properties of CCF.

Table 1. Summary of CCF mechanical properties measured in the previous literatures.

Literature	Density (g/cm ³)	Mechanical Properties
Sihn et al. [15]	0.45	Anisotropic; Young's modulus in x, y, z directions (GPa): 1.09, 1.03, 0.33; Compressive strength in x, y, z directions (MPa): 9.8, 9.2, 3.9
K. Li et al. [16]	0.28	Anisotropic; Young's modulus (GPa): 0.63; Shear modulus (GPa): 0.24
Sihn et al. [17]	0.25	Isotropic; Young's modulus (GPa): 0.95; Compressive strength (MPa): 1.9; Tensile strength (MPa): 0.5
	0.34	Isotropic; Young's modulus (GPa): 1.10; Compressive strength (MPa): 2.3; Tensile strength (MPa): 0.7
Maruyama B et al. [18]	0.62	Young's modulus (GPa): 2.84; Compressive strength (MPa): 24.1
M.D. Sarzynski [19]	0.27	Isotropic; Young's modulus (GPa): 0.37; Tensile strength (MPa): 1.2; Shear modulus (GPa): 0.16; Shear strength (MPa): 1.1
Arand F et al. [20]	0.31	Anisotropic; Young's modulus in x, y, z directions (GPa): 0.47, 0.32, 0.24

The difficulty in establishing the failure criteria of CCF is that CCF is a kind of transverse isotropic cellular foam. Gibson et al. [24] studied the macro failure criteria of both isotropic and anisotropic reticulated vitreous carbon foam (RVC) made of resin. This study measured the stresses in each direction of the isotropic RVC under various multiaxial loads and calculated mean stress (p) and von Mises stress (q) at the time of failure to obtain the isotropic RVC failure surface in $p - q$ space. Equivalent mean stress (\hat{p}) and equivalent von Mises stress (\hat{q}) were proposed according to the definitions of p and q , respectively. It is discovered that the failure surface of anisotropic RVC in $\hat{p} - \hat{q}$ space has a similar shape function to that of isotropic RVC in $p - q$ space. Due to the different mesostructures of RVC and CCF, the failure criteria of RVC cannot be applied to CCF. In addition, the proportion of shear stress in \hat{q} was not thoroughly discussed in their study, which requires modification in the definition of \hat{q} .

Researches on macro failure criteria of carbon foam have been hard to find since Gibson's work. However, there are many studies on the macro failure criteria of other anisotropic foams. M. Alkhader and M. Vural [25,26] studied the macro failure criteria of ideal open-cell anisotropic foams (IOAF) under biaxial and multiaxial loading. Their criteria can accurately predict the test results of Voronoi foam. The IOAF contains no defects, so its tensile strength S_t and compressive strength S_c are equal. Most plastic foams are less sensitive to defects, so the ratio of compressive strength S_c to tensile strength S_t of plastic foam is relatively low ($S_c/S_t = 1.09$ in Voronoi foam), which can be regarded as an approximate IOAF. M. Vural et al. [27,28] studied the macro failure criteria of transversely isotropic PVC foams under multiaxial loading. They have carried out many experiments, and their results have well verified the accuracy of the criteria. Their PVC foam's value

of S_c/S_t is 1.22~1.24, which can be regarded as IOAF. Other scholars [29–32] also studied the criteria of plastic foams (such as metal foams, resin foams, etc.) and achieved valuable results. However, CCF cannot be considered as IOAF, whose value of S_c/S_t is 2.95~3.47 in our study, because CCF is a brittle foam sensitive to defects. Therefore, the criteria of CCF need further study.

According to the achievement of Gibson, the failure criteria of CCF should probably be similar to isotropic cellular foam. Nowadays, isotropic cellular foam failure criteria models are extensively and deeply studied by scholars, among which “Crushable Foam” stands out and is commonly used for foam structure failure analysis. This model is developed by Deshpande and Fleck [33]. In their study, Deshpande and Fleck [33,34] investigated the failure criteria of metallic and PVC foams under uniaxial and hydrostatic compression loading. The failure surface in the $p - q$ space is a semi-ellipse with a central axis on the horizontal axis. Therefore, it is reasonable to assume that the failure surface of CCF in the $\hat{p} - \hat{q}$ space is also a semi-ellipse.

This study aims to establish failure criteria of CCF based on basic macro-mechanical properties that can be used for CCF structure analysis. The novelty in this paper lies in using a modified equivalent von Mises stress method to transform the failure criteria of “Crushable Foam” into CCF, filling the gap of CCF in related fields. Finally, the Abaqus finite element model, including the CCF failure criteria, was established by a user-defined subroutine, and three-point bending tests of the CCF sandwich structure were conducted to verify the criteria.

2. Material and Methods

2.1. Material

The production process of CCF used in this paper was introduced in our previous study [35]. Its mesoscopic structure is presented in Figure 1, which shows that the cells are approximately circular in the section perpendicular to the foaming direction and have higher ellipticity in the section along the foaming path. Therefore, it can be assumed that the CCF we studied is a transverse isotropic foam, and the test results later also confirmed this assumption.

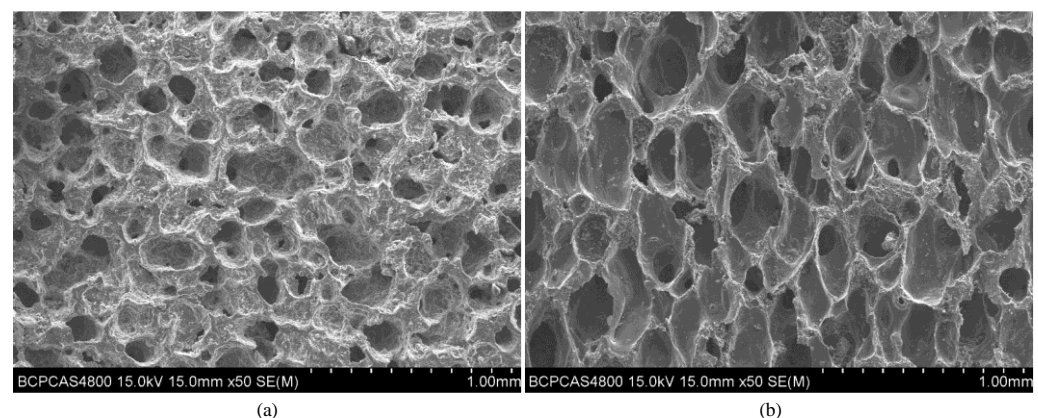


Figure 1. SEM graph of CCF mesostructures: (a) The section is perpendicular to the foaming direction; (b) The section is parallel to the foaming direction.

2.2. Failure Criteria for CCF

The stress–strain relationship of CCF under rectangular coordinate system before failure is

$$\sigma = \begin{bmatrix} \sigma_x \\ \sigma_y \\ \sigma_z \\ \tau_{xy} \\ \tau_{yz} \\ \tau_{xz} \end{bmatrix} = C \begin{bmatrix} \varepsilon_x \\ \varepsilon_y \\ \varepsilon_z \\ \gamma_{xy} \\ \gamma_{yz} \\ \gamma_{xz} \end{bmatrix} = C\varepsilon \tag{1}$$

where σ is the stress vector, ε is the strain vector, C is the stiffness matrix, σ_i and τ_j are the normal stress and shear stress, respectively, with $i = x, y, z$ and $j = xy, yz, xz$. The z direction is defined as the direction of foaming, which is also the one with the strongest mechanical properties. The stiffness matrix C can be expressed as

$$C = \frac{1}{\Omega} \begin{bmatrix} C_{xx} & C_{xy} & C_{xz} & & & \\ C_{yx} & C_{yy} & C_{yz} & & & \\ C_{zx} & C_{zy} & C_{zz} & & & \\ & & & \Omega G_{xy} & & \\ & & & & \Omega G_{yz} & \\ & & & & & \Omega G_{xz} \end{bmatrix} \tag{2}$$

$$C_{xx} = C_{yy} = E_x(1 - \nu_{xz}\nu_{zx}) \quad C_{xy} = C_{yx} = E_x(\nu_{xy} + \nu_{xz}\nu_{zx})$$

$$C_{xz} = E_x(\nu_{xz} + \nu_{xy}\nu_{xz}) \quad C_{yz} = E_x(\nu_{xz} + \nu_{xy}\nu_{xz})$$

$$C_{zz} = E_z(1 - \nu_{xy}^2) \quad E_x = E_y \quad \nu_{xy} = \nu_{yx}$$

$$\frac{\nu_{xz}}{E_x} = \frac{\nu_{zx}}{E_z} \quad \Omega = 1 - \nu_{xy}^2 - 2\nu_{xz}\nu_{zx} - 2\nu_{xy}\nu_{xz}\nu_{zx}$$

where E_i , G_j and ν_j are the Young modulus, shear modulus and Poisson’s ratio, respectively, with $i = x, y, z$ and $j = xy, yz, xz$, where $E_x = E_y$, $G_{xz} = G_{yz}$ and $\nu_{xz} = \nu_{yz}$.

Gibson et al. [24] used the mean stress p and von Mises stress q used to describe the failure criteria of isotropic RVC, which are expressed as

$$p = -\frac{1}{3}(\sigma_x + \sigma_y + \sigma_z) \tag{3}$$

$$q = \frac{1}{\sqrt{2}}\sqrt{((\sigma_x - \sigma_y)^2 + (\sigma_x - \sigma_z)^2 + (\sigma_z - \sigma_y)^2) + 6(\tau_{xy}^2 + \tau_{xz}^2 + \tau_{yz}^2)} \tag{4}$$

and the equivalent mean stress \hat{p} and equivalent von Mises stress \hat{q} based on p and q were further proposed to describe the failure criteria of anisotropic RVC, which are expressed as [24]

$$\hat{p} = -\frac{1}{3}(k_x + k_y + k_z) \tag{5}$$

$$\hat{q} = \frac{1}{\sqrt{2}}\sqrt{(k_x - k_y)^2 + (k_x - k_z)^2 + (k_z - k_y)^2 + (k_{xy}^2 + k_{xz}^2 + k_{yz}^2)} \tag{6}$$

$$k_i = \frac{\sigma_i}{S_{ic}} \quad k_j = \frac{\tau_j}{S_j} \quad i = x, y, z \quad j = xy, yz, xz \tag{7}$$

where S_{ic} is the compressive strength and S_j is the shear strength. Tests were conducted to obtain the failure criteria of anisotropic RVC in $\hat{p} - \hat{q}$ space, including uniaxial compression and tension loading, biaxial compression loading, and axisymmetric loading with all the possible combinations of axial and radial stresses.

The advantage of this method is that failure criteria are characterized by the macroscopic mechanical properties of foam, which is convenient for engineers to measure and analyze the failure of foam structure in finite element software without too much research on the microscopic structure of the foam. However, the contribution of shear stress to foam

failure is understudied. The shear stress item in Equation (6) is $(k_{xy}^2 + k_{xz}^2 + k_{zy}^2)$, and its coefficient is defined as strength factor k_s in this research, whose value is 1 in Equation (6). This k_s reflects the contribution ratio of normal stress and shear stress to foam failure, the smaller k_s is, the less likely shear stress will lead to material failure, and vice versa. Assuming an extreme situation, $k_s = 0$, Equation (6) will have no shear stress item; only the normal stress causes the foam failure, which is impossible. On the contrary, if the value of k_s is vast, then the shear stress will dominate the failure, while the influence of normal stress can be ignored, which is also against common sense. Therefore, the value of k_s must be carefully defined, and its value method will be discussed later in this study. As mentioned above, tests with shear stress are not included in the previous study [24], which means that it can only be proved that Equation (6) is valid in the case of multiaxial loading with only normal stress, and cannot be extended to loading with shear stress.

According to the above reasons, the modified equivalent von Mises stress \hat{q}_m is expressed as

$$\hat{q}_m = \frac{1}{\sqrt{2}} \sqrt{(k_x - k_y)^2 + (k_x - k_z)^2 + (k_z - k_y)^2 + k_s(k_{xy}^2 + k_{xz}^2 + k_{zy}^2)} \quad (8)$$

$$k_i = \begin{cases} \frac{\sigma_i}{S_{it}} & \sigma_i \geq 0 \\ \frac{\sigma_i}{S_{ic}} & \sigma_i \leq 0 \end{cases} \quad i = x, y, z \quad (9)$$

$$k_j = \frac{\tau_j}{S_j} \quad j = xy, yz, zx \quad (10)$$

where S_{it} is the tension strength. In addition to the change of k_s , the expression of Equation (9) in tension is also slightly different from Equation (7), because the difference between tensile strength and compressive strength in CCF huge, while it is small in RVC.

When the CCF is under uniaxial compression loading, the normal stress perpendicular to the loading direction and all shear stresses are 0. In this case, \hat{p} and \hat{q}_m always satisfy $\hat{q}_m = 3\hat{p}$, according to Equations (5) and (8). In particular, $\hat{p} = 1/3$ and $\hat{q}_m = 1$ when the foam fails, no matter which axis is under loading. Similarly, $\hat{p} = -1/3$ and $\hat{q}_m = 1$ when the foam fails under uniaxial tension loading. When the CCF is subjected to compressive shear loading, all stresses except the shear stress on the loaded surface is 0, which makes $\hat{p} = 0$ and $\hat{q}_m = \sqrt{k_s}/2$ when the shear failure occurs. To sum up, the failure surface of CCF in $\hat{p} - \hat{q}_m$ space must go through the point $(-1/3, 1)$ $(1/3, 1)$ and $(0, \sqrt{k_s}/2)$.

The failure surface of the isotropic cellular foam in the $p - q$ space is a semi-ellipse with major axis on horizontal axis [25]. Based on this, it is assumed that the failure surface of CCF in $\hat{p} - \hat{q}_m$ space is also such a semi-ellipse with points $(-1/3, 1)$ $(1/3, 1)$ and $(0, \sqrt{k_s}/2)$ on it; the expression of failure surface in $\hat{p} - \hat{q}_m$ space is

$$\hat{q}_m^2 = a(\hat{p}^2 - 1/9) + 1, \quad k_s = 2(1 - a/9) \quad (11)$$

where a is the shape parameter of the failure surface, whose value needs to be obtained by fitting Equation (16) with at least one additional point on the failure surface. This additional point can only be obtained by multiaxial normal stress loading, because all the failure points of uniaxial loading were used for the acquisition of Equation (16) and the value of k_s is temporarily unknown. Once the value of a is fitted, the value of k_s is determined.

2.3. Experiment for Failure Criteria

The test matrix and specimens are shown in Table 2 and Figure 2, respectively. Uniaxial tests were conducted to obtain the basic macro mechanical properties of CCF in different directions, including tension strength S_{it} , compressive strength S_{ic} , shear strength S_j , Young modulus E_i , shear modulus G_j and Poisson's ratio ν_j , with the z-axis is the foaming direction. All the tests are carried out on the hydraulic fatigue machine. In order to obtain the quasi-static mechanical properties of CCF, the loading speed was set as 1 mm/min, The

relationship between the mechanical properties of CCF and the strain rate can be studied in the future.

Table 2. Test matrix of CCF.

Tests	Reference Standard	Size of Foam (mm ³)	Loading Direction of CCF	Number of Specimens	Aim of Tests
Uniaxial tension	ASTM C297 [36]	30 × 30 × 20	<i>x</i> <i>y</i> <i>z</i>	FT-x1~3 FT-y1~3 FT-z1~3	S_{it}, E_i
Uniaxial compression	ASTM C365 [37] ASTM E132 [38]	30 × 30 × 20	<i>x</i> <i>y</i> <i>z</i>	FCP-x1~5 FCP-y1~5 FCP-z1~5	S_{ic}, E_i, ν_j
Compressive shear	ASTM C273 [39]	150 × 50 × 15	<i>xy</i> <i>xz</i>	CS-xy1~3 CS-xz1~3	S_j, G_j
Passive confining pressure	ASTM C365 [37]	30 × 30 × 20	<i>x</i> <i>y</i> <i>z</i>	SCP-x1~4 SCP-y1~4 SCP-z1~4	Failure stress

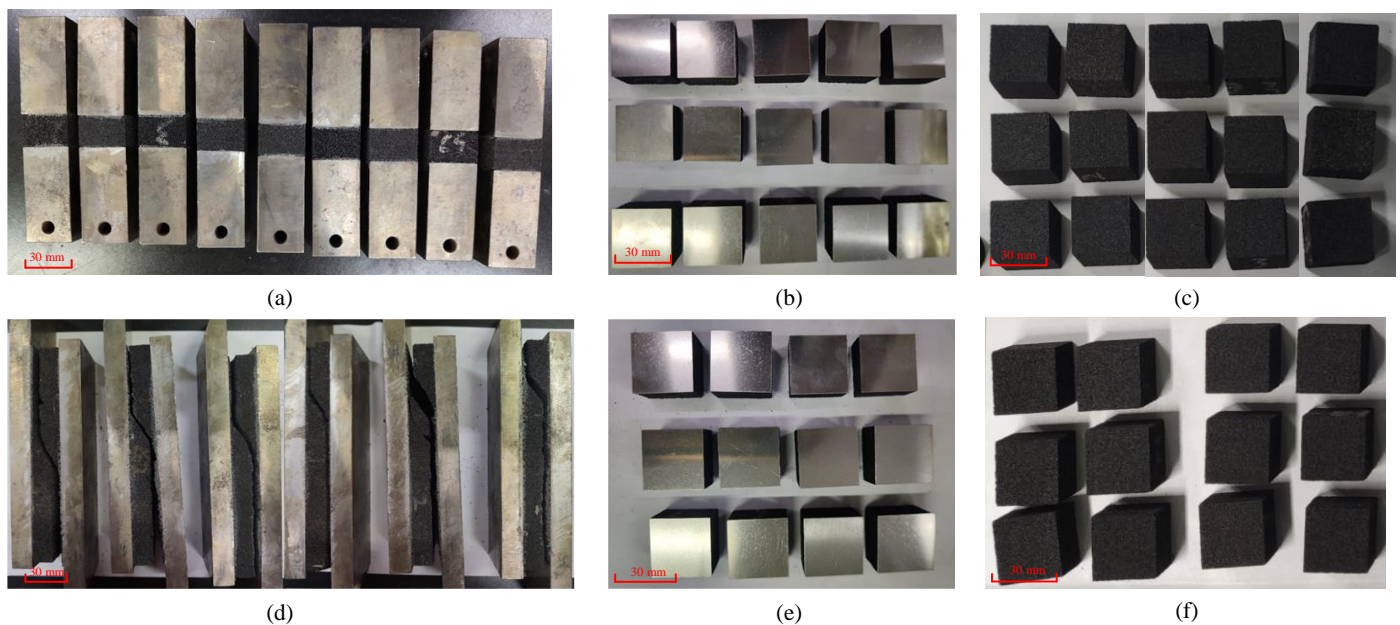


Figure 2. Photograph of specimens: (a) Uniaxial tension specimens; (b) Uniaxial compression specimens; (c) The CCF used in the uniaxial compression specimens; (d) Compressive shear specimens; (e) Passive confining pressure; (f) The CCF used in the passive confining pressure specimens.

It is noted that the standard ASTM C365 [29] proposes that it can determine whether to attach tabs to the compressed surface of the specimen according to material properties. For brittle foams like CCF, it is necessary to attach tabs to obtain real strength, because there must be a large number of broken cell wall structures distributed on the outer surface of the cut CCF specimen. The load-bearing capacity of these cell walls is significantly weaker than that of the intact cell wall. Therefore, if the specimen is directly compressed without the tabs, its damage will occur on the surface of the specimen (as shown in Figure 3a), and the measured strength is relatively lower than the actual value. If tabs are pasted on the foam, the adhesive penetrates into the surface cells and mixes with the carbon skeleton to form an adhesive layer. Since the strength of the adhesive is much greater than the strength of the foam itself, the damage will occur inside the CCF (as shown in Figure 3b), and the measured strength reflects the actual performance of CCFs with intact mesostructure.

In this paper, 1 mm thick steel tabs were attached to the surface of the CCF specimen in compression tests.

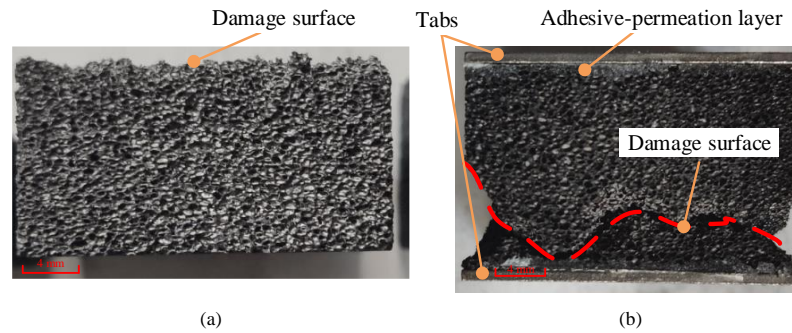


Figure 3. The damage surfaces of CCF in compression tests: (a) Specimen without tabs; (b) Specimen with tabs.

The passive confining pressure test is a simple and effective multiaxial loading test, Kolluri et al. [40] used this method to study the failure criteria of aluminum foam, and Gibson et al. [24] used a similar method to study RVC. This test was conducted to obtain the failure point with multiaxial normal stress loading, as mentioned above. During the test, the specimen is placed in a steel groove. There is an interference fit between the specimen and the groove, and the magnitude of interference is 0.05 mm. Before the specimen is put into the groove, the groove needs to be heated to 80 °C, and the inner wall is coated with lubricating oil. The testing machine applies a compressive load through a compact, as shown in Figure 4. The wall thickness of the groove is 15 mm and is made from steel, so the stiffness of the groove is much larger than that of the CCF specimen. Therefore, it can be considered that the displacement perpendicular to the loading direction of the specimen is limited to 0 during the compression process. When the loading direction is the z direction of CCF, it has $\epsilon_x = \epsilon_y$, and the relationship among σ_x , σ_y , and σ_z before failure is expressed as

$$\sigma_x = \sigma_y = \left(\frac{E_x}{E_z} \right)^2 \frac{\nu_{zx}}{(1 - \nu_{xy})} \sigma_z \tag{12}$$

where σ_z can be obtained from the test. When the loading direction is the x direction of CCF, it has $\epsilon_z = \epsilon_y$, the relationship among σ_x , σ_y , and σ_z before failure is expressed as

$$\sigma_y = \frac{\nu_{xy} + \frac{E_x}{E_z} \nu_{zx}^2}{1 - \frac{E_x}{E_z} \nu_{zx}^2} \sigma_x, \sigma_z = \frac{\frac{E_x}{E_z} \nu_{zx} (1 + \nu_{xy})}{1 - \frac{E_x}{E_z} \nu_{zx}^2} \sigma_x. \tag{13}$$

where σ_x can be obtained from the test. Because of transverse isotropy, an expression similar to Equation (13) can be obtained when the y direction is loaded.

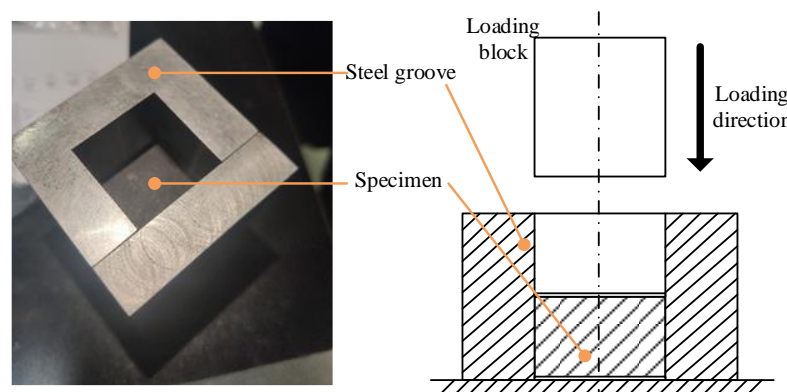


Figure 4. The loading method of passive multiaxial compression tests.

3. Results and Discussion

Figure 5 shows the stress–strain curves of the uniaxial loading tests. It can be seen that CCF exhibits good linear elasticity before failure, so the modulus and strength of CCF correspond to the slope and maximum stress of the linear segment in stress–strain curves, respectively.

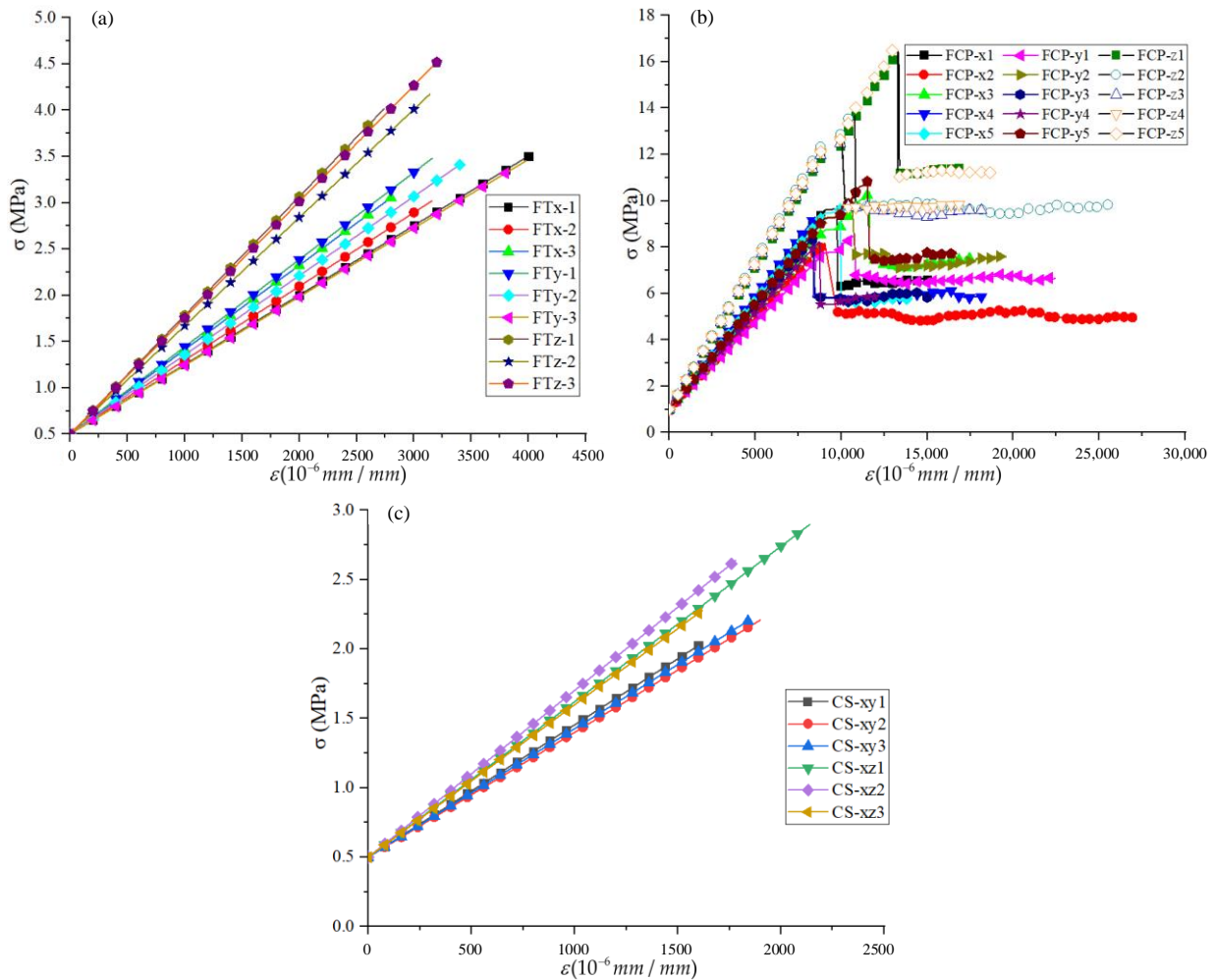


Figure 5. Stress–strain curves of the uniaxial loading tests: (a) Uniaxial tension; (b) Uniaxial compression; (c) Compressive shear in xy and xz plane.

The modulus and strength of CCF are shown in Tables 3 and 4. The tensile modulus and tensile strength in the x direction of CCF are 3.25% and 7.8% different from those in the y direction, respectively, and 33.6% and 24.3% different from those in the z direction. The compressive modulus and compressive strength in the x direction of CCF are 4.90% and 2.22% different from those in the y direction, respectively, while the tensile modulus and tensile strength in the z direction are 28.3% and 35.8% different. It is clear that the difference in mechanical properties between the x and y directions is much smaller than the dispersion. Therefore, the CCF studied in this paper can be considered a transversely isotropic material.

Table 3. Modulus of CCF.

	E_{xt}	E_{yt}	E_{zt}		E_{xc}	E_{yc}	E_{zc}		G_{xy}	G_{xz}
Uniaxial Tension (MPa)	751	943	1283	Uniaxial compression (MPa)	950	746	1232	Compressive shear (MPa)	953	1120
	798	856	1170		792	913	1287		899	1201
	912	742	1256		855	887	1245		925	1098
					977	831	1260			
Average value	820	847	1236		902	857	1258		926	1140
Standard deviation	68	82	48		68	63	19		22	44

Table 4. Strength of CCF.

	S_{xt}	S_{yt}	S_{zt}		S_{xc}	S_{yc}	S_{zc}		S_{xy}	S_{xz}
Uniaxial tension (MPa)	3.51	3.48	4.01	Uniaxial compression (MPa)	9.72	8.55	16.7	Compressive shear (MPa)	2.03	2.89
	3.03	3.42	4.17		8.11	10.1	14.0		2.20	2.64
	3.07	3.46	4.52		10.34	8.31	12.8		2.21	2.29
					9.22	8.22	13.1			
Average value	3.20	3.45	4.23		9.43	9.22	14.7		2.15	2.61
Standard deviation	0.22	0.02	0.21		0.75	1.08	1.74		0.08	0.25

Poisson’s ratio was obtained by simultaneously measuring the lateral and longitudinal displacements of the specimen in uniaxial compression tests with $\nu_{xy} = 0.23$ and $\nu_{zx} = 0.56$. The parameter G_{yz} , S_{yz} , and ν_{zy} were not measured in this study due to the lack of specimen, and their value can be considered equal to G_{xz} , S_{xz} , and ν_{zx} respectively, because of the transversely isotropy of CCF. The results of passive confining pressure tests are listed in Table 5. The stresses perpendicular to the loading direction are calculated by Equations (12) and (13).

Table 5. Failure stresses in passive confining pressure tests.

	σ_x	σ_y	σ_z		σ_x	σ_y	σ_z		σ_x	σ_y	σ_z
x-axis loading (MPa)	−10.2	−5.82	−6.18	y-axis loading (MPa)	−5.41	−9.53	−5.75	z-axis loading (MPa)	−5.67	−5.67	−16.5
	−9.05	−5.14	−5.46		−5.91	−10.4	−6.28		−5.29	−5.29	−15.4
	−9.98	−5.67	−6.03		−5.90	−10.4	−6.27		−5.95	−5.95	−17.3
	−10.6	−5.99	−6.37		−6.58	−11.6	−7.00		−5.02	−5.02	−14.6

So far, the stresses in all directions of CCF failure in uniaxial and multiaxial loading tests have been obtained. The failure points in $\hat{p} - \hat{q}_m$ space of uniaxial tension, uniaxial compression, and passive confining pressure tests, listed in Table 6, were calculated according to Equations (5) and (8)–(10). We mark these points in the $\hat{p} - \hat{q}_m$ coordinate system, as shown in Figure 6. The failure surface is

$$\hat{q}_m^2 = a(\hat{p}^2 - 1/9) + 1 = -1.468\hat{p}^2 + 1.163, a = -1.468 \tag{14}$$

The upper bound of the error band is

$$\hat{q}_m^2 = -1.578\hat{p}^2 + 1.584 \tag{15}$$

The lower bound of the error band is

$$\hat{q}_m^2 = -1.298\hat{p}^2 + 0.812 \tag{16}$$

Then, we got $k_s = 2.326$, which was calculated by Equation (11). So far, the \hat{q}_m of the shear test can be calculated. As shown in Table 6, these failure points are also marked in the $\hat{p} - \hat{q}_m$ coordinates. It can be found that these points are distributed near the failure surface and are all in the error band.

Table 6. The failure points' value of uniaxial tension, uniaxial compression, and passive confining pressure tests. (The data is MPa/MPa).

	\hat{p}	\hat{q}_m		\hat{p}	\hat{q}_m		\hat{p}	\hat{q}_m		\hat{p}	\hat{q}_m
Uniaxial tension	-0.35	1.05	Uniaxial compression	0.35	1.04	Passive confining pressure	0.71	0.60	Compressive shear	0	1.02
	-0.30	0.91		0.29	0.87		0.63	0.53		0	1.11
	-0.31	0.92		0.37	1.11		0.70	0.59		0	1.11
	-0.35	1.05		0.33	0.99		0.74	0.62		0	1.2
	-0.34	1.03		0.35	1.04		0.67	0.56		0	1.09
	-0.35	1.04		0.31	0.92		0.73	0.61		0	0.95
	-0.32	0.95		0.36	1.08		0.72	0.61			
	-0.33	0.99		0.30	0.89		0.81	0.68			
	-0.36	1.07		0.29	0.88		0.78	0.52			
				0.39	1.17		0.73	0.48			
				0.38	1.14		0.82	0.54			
				0.32	0.95		0.69	0.46			
				0.29	0.87						
				0.30	0.89						
		0.38	1.14								

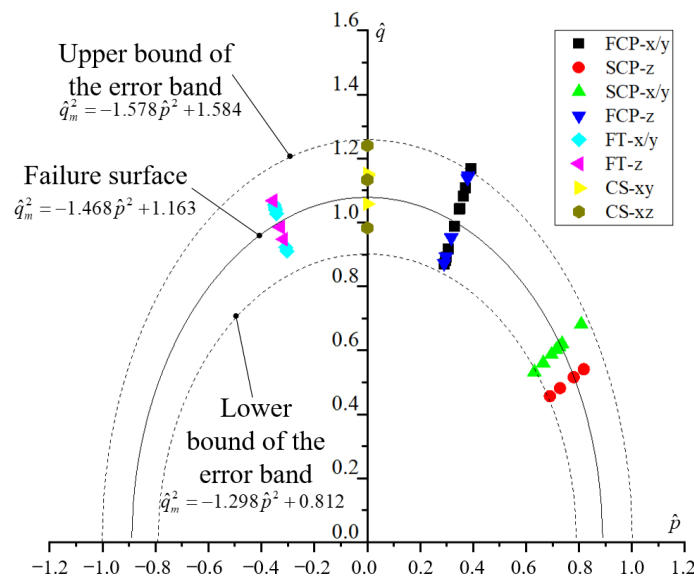


Figure 6. Failure points and surface of CCF in $\hat{p} - \hat{q}_m$ space.

CCF is a brittle foam, which causes its strength to be susceptible to material defects and has a large dispersion of strength. In the $\hat{p} - \hat{q}_m$ space, the failure points under the same loading method are distributed on a straight line passing through the origin of the coordinates. This is because the tests used in this paper belong to the proportional loading of the stress in each direction, and the relationship between \hat{p} and \hat{q}_m always maintains a linear relationship. The error we provide is very significant, and it shows that 95% of the failure points of CCF fall within the range of the error band. When designing the CCF structure in engineering, it should at least ensure that the (\hat{p}, \hat{q}_m) point will not exceed Equation (16).

4. Validation for the Failure Criteria

4.1. 3-Points Bending Tests and Finite Element Model Simulation

Foam materials are often used as the core of sandwich structures under bending load in engineering. Therefore, we conducted three-point bending tests of the CCF sandwich structure and established a finite element model simulating the test process. The effectiveness of the failure criteria of CCF in analyzing the failure of the CCF structure in practice can be verified by comparing the test results and simulation results. The specimens are shown in Figure 7, designed according to ASTM C393 [41], whose numbers are BD-1~5. The thickness of CCF is 15 mm. The thickness direction of the core material is the same as the foaming direction of the foam.



Figure 7. Photograph of 3-points bending specimens.

The face sheet of the CCF sandwich structure is made of carbon fiber/bismaleimide resin composite material (CFRC), the grade is T800/IS2101, whose properties are listed in Table 7. The thickness of each layer is 0.18 mm, and the layout is $[0/45/90/-45]_s$. The maximum load P_{max} and failure mode were obtained in the tests.

Table 7. Mechanical properties of T800/IS2101.

Properties	Direction	Value
Young modulus (GPa)	0°	167
	90°	9.13
Tension strength (MPa)	0°	2761
	90°	38.4
Compressive strength (MPa)	0°	1420
	90°	179
Shear modulus (GPa)	in-plane	4.93
Shear strength (MPa)	in-plane	75

Finite element models (FEMs) based on the three-point bending tests were built to verify the accuracy of the failure criteria of CCF. The CCF constitutive model with failure criteria is established through the VUMAT subroutine, whose process is shown in Figure 8. The CCF failure criteria needs 19 parameters: Young's modulus (E_x, E_y, E_z), shear modulus (G_{xy}, G_{xz}, G_{yz}), Poisson's ratio ($\nu_{xy}, \nu_{zx}, \nu_{zy}$), tension strength (S_{xt}, S_{yt}, S_{zt}), compression strength (S_{xc}, S_{yc}, S_{zc}), shear strength (S_{xy}, S_{xz}, S_{yz}) and shape parameter a . All the parameters above were obtained and can be defined in the subroutine. The Young's modulus, shear modulus and Poisson's ratio form the stiffness matrix C , according to Equation (2). The tension strength, compression strength, shear strength and shape parameter form the failure surface according to Equations (5) and (8)–(11). When the stress state point (\hat{p}, \hat{q}_m) reaches or exceeds the failure surface, the subroutine judges that the CCF has failed. The primary failure mode of the CCF sandwich structure under bending load is a shear failure, which makes the crack continue to expand instead of close after failure. Therefore, there is no compressive stress on the failure section of CCF, so it can be

considered that the failure elements have no bearing capacity and the stiffness matrix can be set to 0. The subroutine was used in the Abaqus explicit dynamic analysis.

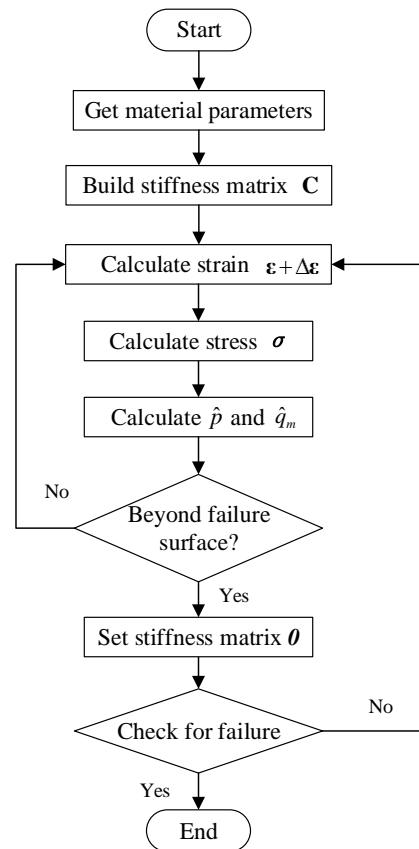


Figure 8. Calculation process of subroutine VUMAT.

The FEM is shown in Figure 9. Eight-node brick element (C3D8R) was used in the whole model, while the stiffness-based hourglass control was used in the CCF core to prevent an hourglass issue in large deformation. The modulus of steel and CFRC were defined by the “isotropy” and “engineering constant” modules, respectively, and their strength were not defined cause the damage only occurred in CCF. The mesh convergence is related to the mesh density. This FEM has 16,000 elements in CFRC and 20,000 in CCF, whose result is 0.8% larger than that of FEM with 12,000 elements in CFRC and 20,000 in CCF, which means the mesh convergence can be guaranteed. The interface between the panels and the core was not damaged, so the elements at the junction of the panels and the core were set as common nodes. The contact surfaces of block-base and block-panel were all defined as a “hard contact” module. A displacement constraint was imposed on the center base to move downward at a speed of 1 mm/min.

A total of four, finite element models were calculated, numbered FEM-1~4. The differences among FEM-1~3 is the damage rule in the subroutine. FEM-1 used the failure surface (Equation (14)) as its damage rule, so that it would calculate the average value of P_{max} in the CCF sandwich structure under three-point bending. FEM-2 and FEM-3 used the upper bound of the error band (Equation (15)) and the lower bound of the error band (Equation (16)) as their damage rules, respectively, so that they would obtain the maximum and minimum values of the error band of P_{max} with a 95% confidence rate. FEM-4 replaces \hat{q}_m with \hat{q} , proposed by Gibson [24], to compare the difference in accuracy between our method and previous methods. It is worth noting that Equation (14) is obtained through the test of only normal stress loading, which has no concern with the value of k_s , so the equations of the failure surface in $\hat{p} - \hat{q}$ space and $\hat{p} - \hat{q}_m$ space were the same. Therefore,

the damage rule used in FEM-4 was also Equation (14). The differences among FEM-1~4 are listed in Table 8.

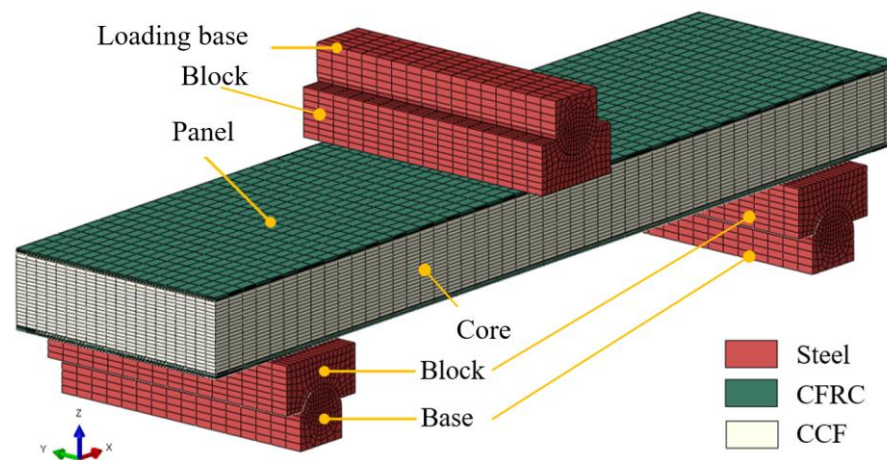


Figure 9. Abaqus explicit dynamic analysis model of 3-points bending.

Table 8. The differences among FEM-1~4.

FEM	Damage Rule	Stress Space
FEM-1	The failure surface (Equation (14))	$\hat{p} - \hat{q}_m$ (Equations (5) and (8))
FEM-2	The upper bound of the error band of failure surface (Equation (15))	$\hat{p} - \hat{q}_m$ (Equations (5) and (8))
FEM-3	The lower bound of the error band of failure surface (Equation (16))	$\hat{p} - \hat{q}_m$ (Equations (5) and (8))
FEM-4	The failure surface (Equation (14))	$\hat{p} - \hat{q}$ (Equations (5) and (8))

4.2. Validation Results

Load–displacement curves and P_{max} of three-point bending tests and simulations are shown in Figure 10. FEM-1~4 overlap because the difference between these finite element models is the failure criteria used to calculate P_{max} , and other parameters in the model are the same. It can be seen that all the P_{max} values measured by the test (3933 N, 3640 N, 3657 N, 3269 N, 3091 N) were between the maximum value (4297 N) and minimum value (3085 N), which, respectively, were calculated by FEM-2 and FEM-3. The mean value of P_{max} calculated by FEM-1 (3684 N) is only 4.7% larger than the mean value of P_{max} measured by the test (3518 N), which shows that the failure criteria proposed in this paper have sufficient precision. The P_{max} calculated by the Gibson method (FEM-4) is 4808 N, which is 30.5% larger than the mean value of P_{max} measured by the test.

The mechanism of FEM-4 producing larger errors is as follows: by substituting the stresses at the initial failure node in FEM-1 (as shown in Table 9) into Equations (5) and (6), we then obtained $\hat{p} = 0.0439$ and $\hat{q} = 0.6359$ in the Gibson method, respectively. By substituting the \hat{p} and \hat{q} into the failure surface (Equation (14)), we then obtained $\hat{q}^2 = 0.4043 < 1.1602 = -1.468\hat{p}^2 + 1.163$. This means that when our failure criteria determine that the CCF is damaged, Gibson's failure criteria also considers that the CCF is yet to be damaged. This is due to the large difference between \hat{q} and \hat{q}_m that the k_s in \hat{q} is defaulted to be 1 by Gibson, and the k_s in \hat{q}_m is 2.326 according to our study. The k_s represents the contribution rate of shear stress to failure. Thus, in the case of shear stress dominated failure, the failure load calculated by \hat{q} must be greater than the shear load calculated by \hat{q}_m . This shows that the modified equivalent von Mises stress \hat{q}_m that we proposed can make the failure criteria have better accuracy.

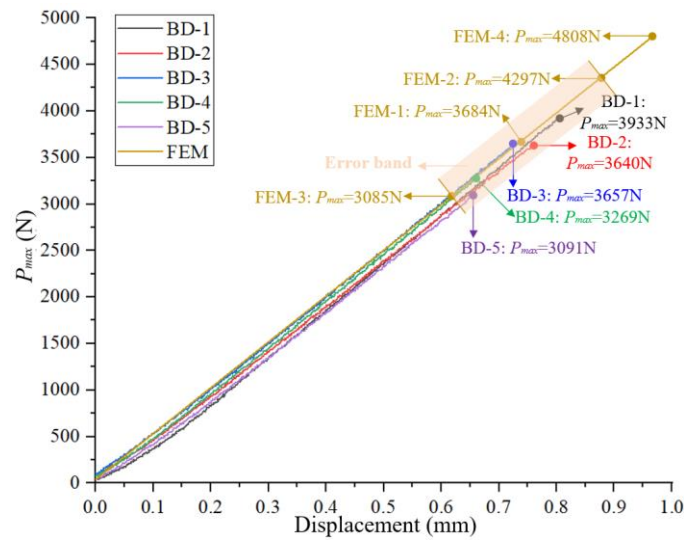


Figure 10. Load–displacement curves and P_{max} of 3-points bending tests and simulations.

Table 9. Stresses at the initial failure node in FEM-1.

	σ_x	σ_y	σ_z	τ_{xy}	τ_{xz}	τ_{yz}
Stress (MPa)	1.840	0.128	−1.136	0.005	−2.168	0.150

The failure mode of the three-point bending test and its finite element model are shown in Figure 11. It can be seen that the failure mode of the CCF sandwich structure in the three-point bending test is the shear damage of the core material, and longitudinal cracks are generated in the core material and propagate to the interface between the sheet and the core on both sides. The FEM can simulate the initial damage and the propagation process. However, the longitudinal cracks in FEM-1 are along the thickness direction, while the longitudinal cracks in the test results have a certain angle with the thickness direction. This shows that, although our FEM can accurately calculate the load at the initial damage, it failed to simulate the damage propagation. This may be because the VUMAT subroutine that we used cannot simulate the mechanical behavior of CCF well after damage, and further research is needed in the future.

The shear stress τ_{xz} dominated the failure of CCF, so Figure 12 shows the contours of τ_{xz} before and after the initial damage of FEM-1. It can be seen from Figure 12a that the initial damage occurred on the lower surface under tension. It can be seen from Table 9 that τ_{xz} is smaller than S_{xz} (2.61 MPa) measured in the test. This is because $\sigma_x/S_{xt} = 0.575$ and the contribution of σ_x to damage cannot be ignored. Figure 12b shows the stress contour of the damaged unit after initial damage. It can be found that the position of the unit with the largest τ_{xz} moves upward, so the damaged element propagated upward. At the same time, the maximum τ_{xz} increases (2.309 MPa), which may be caused by the stress concentration and the decrease of the shear plane in the CCF.

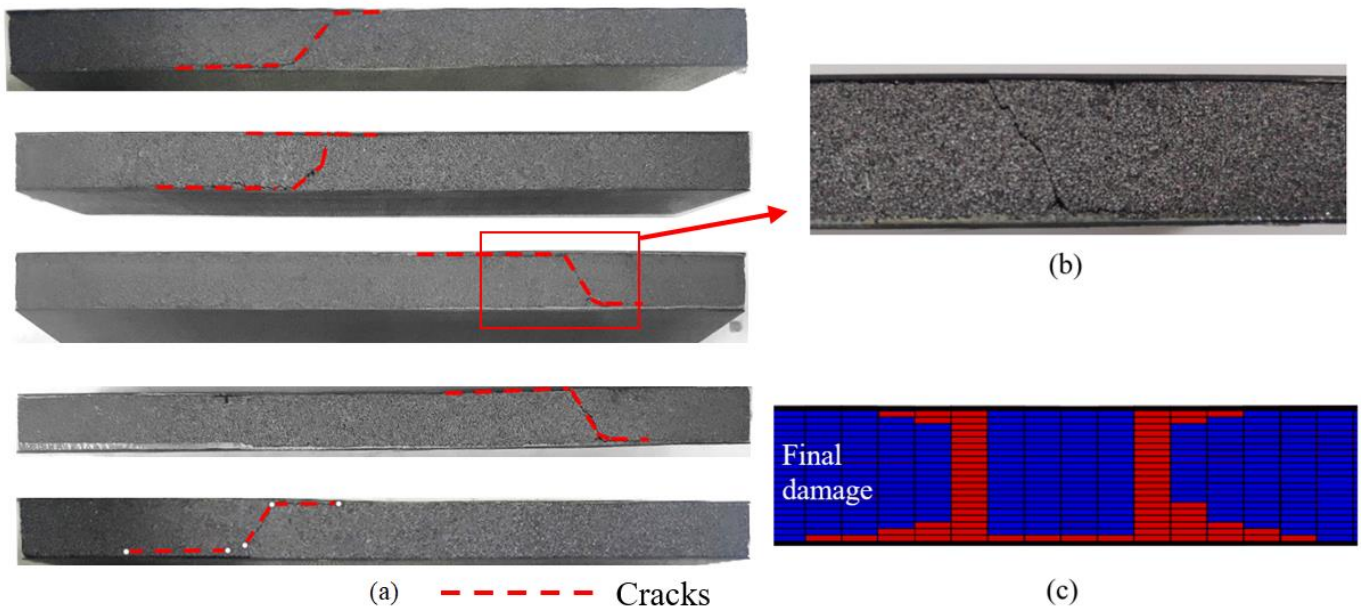


Figure 11. Failure mode of three-point bending test and its finite element model: (a) Failure mode of all the specimens; (b) Details of damage; (c) The final damage obtained by the FEM-1.

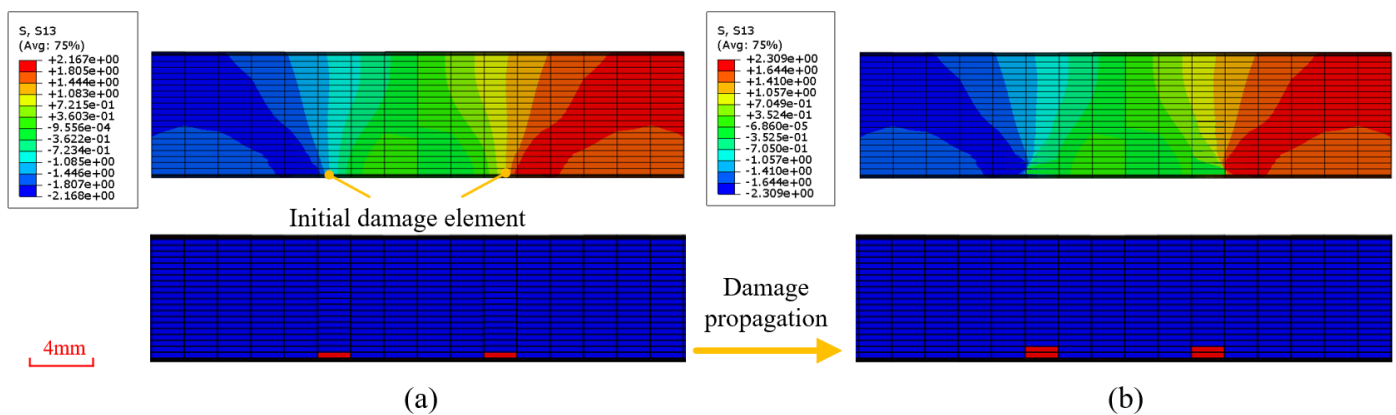


Figure 12. The local contours of shear stress τ_{xz} of CCF in FEM-1: (a) The contour when initial damage occurred; (b) The contour when damage propagated.

5. Conclusions

Failure criteria of core-based carbon foam are proposed in this paper. It is applied to a finite element model and can be summarized as follows:

- The failure criteria can be obtained by the following steps: (a) Obtain the basic mechanical properties of CCF in all directions through uniaxial loading tests, including strength, modulus, and Poisson’s ratio, and then we obtain \hat{p} and \hat{q}_m independent of shear stress; (b) Get the equation of failure surface in $\hat{p} - \hat{q}_m$ space by fitting the results of multiaxial loading tests without shear load; (c) Calculate the k_s according to the equation of failure surface, and then we obtain the complete equations of \hat{p} and \hat{q}_m ;
- A large number of material-level tests were carried out to measure the basic mechanical properties of CCF, and the equation of the failure surface and its upper and lower bounds of error bands were obtained;
- CCF constitutive model with failure criteria was established through the VUMAT subroutine. It was used to predict the maximum failure load and failure mode of the CCF sandwich structure under a three-point bending load. The analysis results are in good agreement with experimental results and have higher accuracy than previous methods.

In conclusion, our CCF failure criteria have sufficient precision and can be obtained from simple macro-mechanical tests, and they are also available for engineering design analysis.

Author Contributions: Conceptualization, Q.Z.; methodology, Q.Z., K.L. and X.C.; software, Q.Z. and P.Y.; validation, Q.Z., P.Y., K.L. and X.G.; data curation, Q.Z. and X.G.; writing—original draft preparation, Q.Z.; writing—review and editing, Q.Z., X.C., P.Y., X.G., K.L. All authors have read and agreed to the published version of the manuscript.

Funding: This research received no external funding.

Data Availability Statement: Not applicable.

Conflicts of Interest: The authors declare no conflict of interest.

References

1. Chen, C.; Kennel, E.B.; Stiller, A.H.; Stansberry, P.G.; Zondlo, J.W. Carbon foam derived from various precursors. *Carbon* **2006**, *44*, 1535–1543. [[CrossRef](#)]
2. Inagaki, M.; Qiu, J.; Guo, Q. Carbon foam: Preparation and application. *Carbon* **2015**, *87*, 128–152. [[CrossRef](#)]
3. Su, R.; Wang, X.; Wang, D.; Li, L.; Liang, G.; Zheng, Z.; Li, K. Preparation of carbon foam-reinforced carbon aerogels and their copyrolysis mechanism. *Microporous Mesoporous Mater.* **2021**, *319*, 111059. [[CrossRef](#)]
4. Eck, J.; Balat-Pichelin, M. Study of carbon erosion under ion bombardment at high temperature: Application to the thermal protection system of Solar Probe+. *Vacuum* **2010**, *85*, 380–389. [[CrossRef](#)]
5. Heisler, E.; Abel, E.; Congdon, E.; Eby, D. Full scale thermal simulator development for the solar probe plus thermal protection system. In Proceedings of the 2017 IEEE Aerospace Conference, Big Sky, MT, USA, 4–11 March 2017.
6. Grujicic, M.; Zhao, C.; Biggers, S.; Kennedy, J.; Morgan, D. Suitability of a Coal-Derived Carbon-Based Foam for use in Thermal Protection Systems of Common Aero Vehicles. *Multidiscip. Model. Mater. Struct.* **2007**, *3*, 1–26. [[CrossRef](#)]
7. Fawcett, R.; Hornick, J.; Backlund, D.; Pichon, T.; Foucault, A.; Ellis, R. Advanced 3rd Stage (A3S) Carbon-Carbon Exit Cone. In Proceedings of the 44th AIAA/ASME/SAE/ASEE Joint Propulsion Conference & Exhibit, Hartford, CT, USA, 21–23 July 2008.
8. Suzuki, T.; Aoki, T.; Ogasawara, T.; Fujita, K. Nonablative lightweight thermal protection system for Mars Aeroflyby Sample collection mission. *Acta Astronaut.* **2017**, *136*, 407–420. [[CrossRef](#)]
9. Ogasawara, T.; Ayabe, S.; Ishida, Y.; Aoki, T.; Kubota, Y. Heat-resistant sandwich structure with carbon fiber-polyimide composite faces and a carbon foam core. *Compos. Part A Appl. Sci. Manuf.* **2018**, *114*, 352–359. [[CrossRef](#)]
10. Kubota, Y.; Miyamoto, O.; Aoki, T.; Ishida, Y.; Ogasawara, T.; Umezu, S. New thermal protection system using high-temperature carbon fibre-reinforced plastic sandwich panel. *Acta Astronaut.* **2019**, *160*, 519–526. [[CrossRef](#)]
11. Alifanov, O.M.; Budnik, S.A.; Nenarokomov, A.V.; Salosina, M.O. Design of thermal protection based on open cell carbon foam structure optimization. *Appl. Therm. Eng.* **2020**, *173*, 115252. [[CrossRef](#)]
12. Liu, X.S.; Fu, Q.G.; Zhang, J.P.; Tong, M.D.; Ma, W.H. Design of a novel all-carbon multi-layer structure with excellent thermal protection performance based on carbon/carbon composites and carbon foam. *Ceram. Int.* **2020**, *46*, 28887–28893. [[CrossRef](#)]
13. Li, Y.; Xiao, Y.; Yu, L.; Ji, K.; Li, D. A review on the tooling technologies for composites manufacturing of aerospace structures: Materials, structures and processes. *Compos. Part A Appl. Sci. Manuf.* **2022**, *154*, 106762. [[CrossRef](#)]
14. Pahuja, R.; Ramulu, M. Study of surface topography in Abrasive Water Jet machining of carbon foam and morphological characterization using Discrete Wavelet Transform. *J. Mater. Process. Technol.* **2019**, *273*, 116249. [[CrossRef](#)]
15. Sih, S.; Rice, B.P. Sandwich construction with carbon foam core materials. *J. Compos. Mater.* **2003**, *37*, 1319–1336. [[CrossRef](#)]
16. Li, K.; Gao, X.L.; Roy, A.K. Micromechanical modeling of three-dimensional open-cell foams using the matrix method for spatial frames. *Compos. Part B Eng.* **2005**, *36*, 249–262. [[CrossRef](#)]
17. Sih, S.; Roy, A.K. Modeling and prediction of bulk properties of open-cell carbon foam. *J. Mech. Phys. Solids* **2004**, *52*, 167–191. [[CrossRef](#)]
18. Maruyama, B.; Spowart, J.E.; Hooper, D.J.; Mullens, H.M.; Druma, A.M.; Druma, C.; Alam, M.K. A new technique for obtaining three-dimensional structures in pitch-based carbon foams. *Scr. Mater.* **2006**, *54*, 1709–1713. [[CrossRef](#)]
19. Sarzynski, M.D. Carbon Foam Characterization: Sandwich Flexure, Tensile and Shear Response. Doctoral Dissertation, Texas A&M University, College Station, TX, USA, 2004.
20. Arand, F.; Hesser, J. Quantitative morphological analysis and digital modeling of polydisperse anisotropic carbon foam. *Carbon* **2018**, *136*, 11–20. [[CrossRef](#)]
21. Druma, C.; Alam, M.K.; Druma, A.M. Finite element model of thermal transport in carbon foams. *J. Sandw. Struct. Mater.* **2004**, *6*, 527–540. [[CrossRef](#)]
22. Yu, Q.; Thompson, B.E.; Straatman, A.G. A unit cube-based model for heat transfer and fluid flow in porous carbon foam. *J. Heat Transfer* **2006**, *128*, 352–360. [[CrossRef](#)]
23. Anghelescu, M.; Alam, K. Finite element modeling of forced convection heat transfer in carbon foams. In Proceedings of the ASME International Mechanical Engineering Congress and Exposition, Chicago, IL, USA, 5–10 November 2006.

24. Triantafillou, T.C.; Gibson, L.J. Multiaxial failure criteria for brittle foams. *Int. J. Mech. Sci.* **1990**, *32*, 479–496. [[CrossRef](#)]
25. Alkhader, M.; Vural, M. An energy-based anisotropic yield criterion for cellular solids and validation by biaxial FE simulations. *J. Mech. Phys. Solids* **2009**, *57*, 871–890. [[CrossRef](#)]
26. Alkhader, M.; Vural, M. A plasticity model for pressure-dependent anisotropic cellular solids. *Int. J. Plast.* **2010**, *26*, 1591–1605. [[CrossRef](#)]
27. Ayyagari, R.S.; Vural, M. Multiaxial yield surface of transversely isotropic foams: Part I—Modeling. *J. Mech. Phys. Solids* **2015**, *74*, 49–67. [[CrossRef](#)]
28. Shafiq, M.; Ayyagari, R.S.; Ehaab, M.; Vural, M. Multiaxial yield surface of transversely isotropic foams: Part II—Experimental. *J. Mech. Phys. Solids* **2015**, *76*, 224–236. [[CrossRef](#)]
29. Gioux, G.; McCormack, T.M.; Gibson, L.J. Failure of aluminum foams under multiaxial loads. *Int. J. Mech. Sci.* **2000**, *42*, 1097–1117. [[CrossRef](#)]
30. Doyoyo, M.; Wierzbicki, T. Experimental studies on the yield behavior of ductile and brittle aluminum foams. *Int. J. Plast.* **2003**, *19*, 1195–1214. [[CrossRef](#)]
31. Tita, V.; Caliri Júnior, M.F. Numerical simulation of anisotropic polymeric foams. *Lat. Am. J. Solids Struct.* **2012**, *9*, 1–21. [[CrossRef](#)]
32. Mosleh, Y.; Bosche, K.V.; Depreitere, B.; Sloten, J.V.; Verpoest, I.; Ivens, J. Effect of polymer foam anisotropy on energy absorption during combined shear-compression loading. *J. Cell. Plast.* **2018**, *54*, 597–613. [[CrossRef](#)]
33. Deshpande, V.S.; Fleck, N.A. Isotropic constitutive models for metallic foams. *J. Mech. Phys. Solids* **2000**, *48*, 1253–1283. [[CrossRef](#)]
34. Deshpande, V.S.; Fleck, N.A. Multi-axial yield behaviour of polymer foams. *Acta Mater.* **2001**, *49*, 1859–1866. [[CrossRef](#)]
35. Wang, D.; Zhuang, Q.; Li, K.; Wang, Y. Study on Correlation of Mechanical and Thermal Properties of Coal-Based Carbon Foam with the Weight Loss Rate after Oxidation. *Materials* **2022**, *15*, 4887. [[CrossRef](#)] [[PubMed](#)]
36. *ASTM C297/C297M—16*; Standard Test Method for Flatwise Tensile Strength of Sandwich Constructions. ASTM International: West Conshohocken, PA, USA, 2016.
37. *ASTM-C365/C365M—16*; Standard Test Method for Flatwise Compressive Properties of Sandwich Cores. ASTM International: West Conshohocken, PA, USA, 2016.
38. *ASTM-E132/E132M—17*; Standard Test Method for Poisson’s Ratio at Room Temperature. ASTM International: West Conshohocken, PA, USA, 2017.
39. *ASTM C273/C273M—11*; Standard Test Method for Shear Properties of Sandwich Core Materials. ASTM International: West Conshohocken, PA, USA, 2011.
40. Kolluri, M.; Karthikeyan, S.; Ramamurty, U. Effect of lateral constraint on the mechanical properties of a closed-cell Al foam: I. Experiments. *Metall. Mater. Trans. A* **2007**, *38*, 2006–2013. [[CrossRef](#)]
41. *ASTM C393/C393M—11*; Standard Test Method for Core Shear Properties of Sandwich Constructions by Beam Flexure. ASTM International: West Conshohocken, PA, USA, 2012.

Disclaimer/Publisher’s Note: The statements, opinions and data contained in all publications are solely those of the individual author(s) and contributor(s) and not of MDPI and/or the editor(s). MDPI and/or the editor(s) disclaim responsibility for any injury to people or property resulting from any ideas, methods, instructions or products referred to in the content.